

Energy exchange in a dense urban environment – part I: temporal variability of long-term observations in central London

Article

Published Version

Open Access

Kotthaus, S. and Grimmond, C. S. B. ORCID:
<https://orcid.org/0000-0002-3166-9415> (2014) Energy exchange in a dense urban environment – part I: temporal variability of long-term observations in central London. *Urban Climate*, 10 (2). pp. 261-280. ISSN 2212-0955 doi:
<https://doi.org/10.1016/j.uclim.2013.10.002> Available at
<https://centaur.reading.ac.uk/36103/>

It is advisable to refer to the publisher's version if you intend to cite from the work. See [Guidance on citing](#).

To link to this article DOI: <http://dx.doi.org/10.1016/j.uclim.2013.10.002>

Publisher: Elsevier

All outputs in CentAUR are protected by Intellectual Property Rights law, including copyright law. Copyright and IPR is retained by the creators or other copyright holders. Terms and conditions for use of this material are defined in the [End User Agreement](#).

www.reading.ac.uk/centaur

CentAUR

Central Archive at the University of Reading

Reading's research outputs online

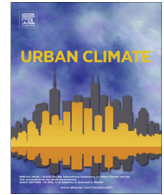


ELSEVIER

Contents lists available at ScienceDirect

Urban Climate

journal homepage: www.elsevier.com/locate/uclim



Energy exchange in a dense urban environment – Part I: Temporal variability of long-term observations in central London



Simone Kotthaus*, C.S.B. Grimmond

*Earth and Environmental Dynamics, Department of Geography, King's College London, The Strand, London WC2R 2LS, UK
Department of Meteorology, University of Reading, Earley Gate, PO Box 243, Reading RG6 6BB, UK*

ARTICLE INFO

Article history:

Received 15 March 2013
Revised 19 August 2013
Accepted 8 October 2013

Keywords:

Radiation
Sensible heat flux
Evaporation
Human activities
Urban eddy covariance
ClearFlo

ABSTRACT

Though anthropogenic impacts on boundary layer climates are expected to be large in dense urban areas, to date very few studies of energy flux observations are available. We report on 3.5 years of measurements gathered in central London, UK. Radiometer and eddy covariance observations at two adjacent sites, at different heights, were analysed at various temporal scales and with respect to meteorological conditions, such as cloud cover. Although the evaporative flux is generally small due to low moisture availability and a predominately impervious surface, the enhancement following rainfall usually lasts for 12–18 h. As both the latent and sensible heat fluxes are larger in the afternoon, they maintain a relatively consistent Bowen ratio throughout the middle of the day. Strong storage and anthropogenic heat fluxes sustain high and persistently positive sensible heat fluxes. At the monthly time scale, the urban surface often loses more energy by this turbulent heat flux than is gained from net all-wave radiation. Auxiliary anthropogenic heat flux information suggest human activities in the study area are sufficient to provide this energy.

© 2013 Elsevier B.V. All rights reserved.

1. Introduction

Urban areas present a special challenge for understanding near-surface climate conditions in the atmospheric boundary layer. Human activities, which vary with time, combined with the highly

* Corresponding author at: Department of Meteorology, University of Reading, Earley Gate, PO Box 243, Reading RG6 6BB, UK. Tel.: +44 118 378 5419.

E-mail address: s.kotthaus@reading.ac.uk (S. Kotthaus).

complex and heterogeneous surface structure across cities impact exchanges of energy and pollutants. Observations offer a crucial means to improve the understanding and interpretation of atmospheric processes, and provide the basis for model development and evaluation. In order to take into account this diversity, micrometeorological research needs to address a variety of different urban land uses (Arnfield, 2003).

Grimmond (2006) and the WMO (Grimmond et al., 2010) identify the need for more urban energy flux observations that cover long time periods and a greater variety of locations in order to study the full spectrum of urban influences and also seasonal variations of the urban energy balance influenced by distinct weather/climate conditions and surface properties. Although more flux sites have been installed in the last decade (Grimmond, 2006), the coverage does not yet address the diversity or range of urban areas globally. As Goldbach and Kuttler (2012) list, recent turbulent flux observations include European cities; viz, Basel, Switzerland (Christen and Vogt, 2004), Marseille, France (Grimmond et al., 2004), Toulouse, France (Masson et al., 2008), Łódź, Poland (Offerle et al., 2006a,b; Pawlak et al., 2011; Fortuniak et al., 2012), Helsinki, Finland (Vesala et al., 2008), Essen, Germany (Weber and Kordowski, 2010) and Oberhausen, Germany (Goldbach and Kuttler, 2012), while earlier research focused largely on cities in North America (e.g. Grimmond and Oke, 1995, 2002). New insights are also being gained from turbulent surface exchange studies located in different climates and synoptic conditions (e.g. Tokyo, Japan, Moriwaki and Kanda, 2004; Ouagadougou, Burkina Faso, Offerle et al., 2005; Melbourne, Australia, Coutts et al., 2007; Helsinki, Finland, Järvi et al., 2009; Cairo, Egypt, Frey et al., 2011). Data sets for longer time periods are allowing seasonal and annual variability to be examined (e.g. Christen and Vogt, 2004; Offerle et al., 2006a; Coutts et al., 2007; Järvi et al., 2009). Most study sites though are still located in suburban, residential or industrial areas. Thus our knowledge of surface exchange processes in dense city centres remains limited (e.g. Basel, Christen and Vogt, 2004; Helsinki, Nordbo et al., 2012). Further, we might expect that locations where large and dense urban populations work and live are areas of some of the most extreme urban influences.

The focus of the current study is London, UK, one of the European Union's most densely populated cities with a population of over 8.2 million (Greater London, mid-2011 census, Office for National Statistics, 2012). The history of urban climate studies in London reaches back to the historical contributions of Luke Howard starting in the early 1800s (Howard, 1818, Howard, 1833). Since then, the UK capital has undergone extensive growth. Recent urban climate observations in London have been concerned with dispersion of pollutants (DAPPLE, Arnold et al., 2004; Robins, 2008; REPARTEE, Harrison et al., 2012) and the applicability of similarity theory in the urban environment (Wood et al., 2010). Wood et al. (2010) report observations undertaken at 190 m above ground (BT tower) which, in addition to heat and momentum flux measurements, also include observations of atmospheric chemistry (Langford et al., 2010; Helfter et al., 2011). In contrast to the observations on the BT tower, the measurements presented in this study are in the very centre of the city, at a lower measurement height. Thus the source area is more homogeneous and reflects London's central business district, designated the 'Central Activities Zone' (CAZ, Fig. 1a) by the Greater London Authority (GLA, 2011). The measurements are conducted right next to Somerset House, which in the nineteenth century housed the Royal Society. This is where Luke Howard's 'urban' sensor was located (Mills, 2008) that enabled him to identify the urban warming effect.

The objective of this paper is to describe the temporal characteristics of observations undertaken in the dense urban city centre of London. The impact of the spatial heterogeneity of the urban surface on the flux observations is addressed in a companion paper (Kotthaus and Grimmond, 2013), based on footprint analysis and a comparison of two adjacent sites. Here, data collection and processing methods, including the auxiliary data of an anthropogenic heat flux model, are presented (Section 2). The results are analysed (Section 3) in terms of the seasonal and monthly behaviour of the energy balance components. The role of precipitation and the temporal evolution of energy partitioning over the course of a day are also studied. Our key findings (Section 4) contribute to current understanding of the microclimate of highly urbanised environments.

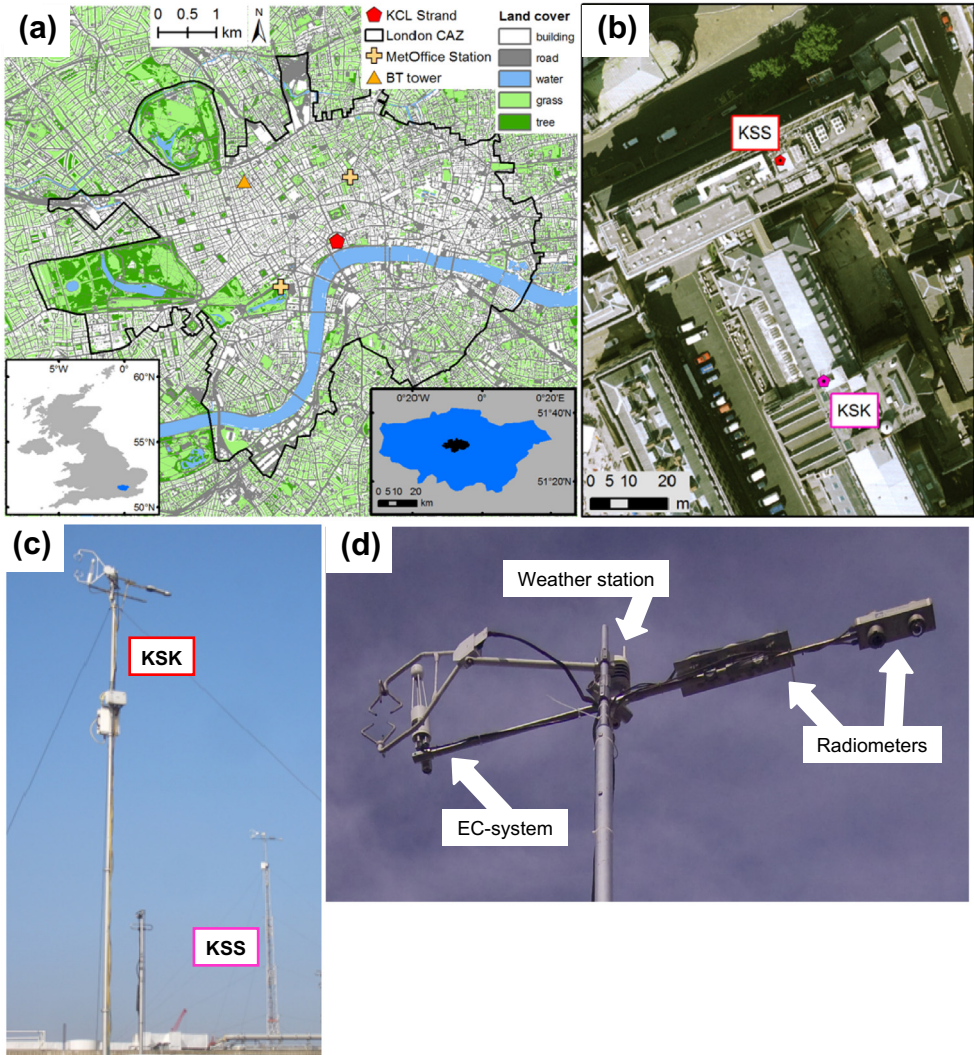


Fig. 1. (a) Land cover map (based on OS MasterMap) of the Central Activities Zone (CAZ) and vicinity of Central London with locations of KCL Strand, Met Office measurement stations and BT Tower. In this study observations from St. James's Park are used. The location of CAZ (indicated in black) within the Greater London area (blue) is shown in the right inset and this within Great Britain in the left inset; (b) Aerial photo (NERC ARSF 2008) showing locations of KSS and KSK towers (see Section 2.1); (c) Photo of KSK mast and KSS tower (taken in 2012); (d) Setup at KSS tower with EC-system, weather station and radiometers (setup at KSK setup similar, Table 1). (For interpretation of the references to color in this figure legend, the reader is referred to the web version of this article.)

2. Methods

Investigating surface energy exchange in urban areas requires a combination of different methodologies in order to estimate the components of the surface volume energy balance (Oke, 1987):

$$Q^* + Q_F = Q_H + Q_E + \Delta Q_S + \Delta Q_A.$$

In addition to radiative energy input given by the net all-wave radiation Q^* , the anthropogenic heat flux Q_F plays a significant role in many urban areas. Available energy is partitioned into the turbulent fluxes of sensible heat Q_H and latent heat Q_E . The storage heat flux ΔQ_S is related to the net heating and

cooling of the urban canopy volume. Finally, ΔQ_A describes net energy exchanges via vertical or horizontal advection.

In the present study, net all-wave radiation as well as sensible and latent heat fluxes were derived from *in-situ* observations. Anthropogenic heat flux was incorporated in the analysis using estimates from a top-down approach based on energy consumption (*GreaterQf* model, [Iamarino et al., 2012](#)). The storage heat flux is very difficult to measure directly ([Grimmond, 1992](#)), requiring extensive observations that cover the diversity of buildings, canyons and other elements of the urban canopy volume. Hence it is often calculated as the residual Q_{RES} of the energy balance equation assuming a negligible advective flux ΔQ_A . Cautious analysis of this Q_{RES} is required as it incorporates uncertainties of all other fluxes and implies energy balance closure ([Grimmond and Oke, 1999](#); [Foken et al., 2006](#)). The interpretation of the various fluxes as a ‘balance’ assumes that the radiation, anthropogenic heat and turbulent fluxes have spatially consistent source areas or that the surface characteristics within the source areas of each are spatially representative ([Roberts, 2010](#)).

2.1. Measurement site

The study area is located in the ‘Central Activities Zone’ (CAZ) of London, UK, the destination of many commuters in (and to) the capital. While about 275 000 people live in this area ([GLA, 2011](#)), the daytime population is several times higher. The CAZ covers parts of the three busiest London boroughs with daytime populations of 520 000 (Camden), 603 000 (City of London), and 987 000 (Westminster), respectively ([GLA, 2012](#)).

London has a temperate marine climate that experiences mid-latitude low pressure systems, inducing precipitation, clouds and increased wind speeds ([MetOffice, 2012](#)). Typically these frontal systems have a somewhat diminished intensity when they reach the South-East of England on their passage from the west. As this part of the British Isles is closest to the European mainland, continental weather conditions occasionally influence the area. Due to this proximity and the sheltering effect by the UK landmass from mid-latitude cyclones, the South-East receives less precipitation than the rest of the country ([MetOffice, 2012](#)). It does, however, experience added convective activity and the large area of Greater London (1570 km²) might account for some increase in cloud cover and convective precipitation ([Atkinson, 1969](#)). On average¹, the annual rainfall in central London is 570 mm and mean daily (24 h) temperature ranges from about 5 °C in January to 19 °C in July. The area is on occasion exposed to sea breezes ([Bohnenstengel et al., 2011](#); [Chemel and Sokhi, 2012](#)).

Two measurement towers, referred to as KSS and KSK, are located at the Strand Campus of King’s College London (KCL, 51°30’N, 0°7’W), approximately 60 m apart ([Fig. 1](#)). [Loridan et al. \(2013\)](#) classify the surrounding area as a “High Density” UZE (Urban Zone for Energy partitioning, [Loridan and Grimmond, 2012](#)). From the image-based classification approach of [Stewart and Oke \(2012\)](#) it is “compact midrise” LCZ (Local Climate Zone).

At both sites, sensors are mounted on the top of extendable towers (KSK: single tube mast, Clark Masts CSQ T97/HP; KSS: triangular tower, Aluma T45-H), which are installed on top of buildings. The measurement height above ground level (agl) is 49 m at KSS and 39 m at KSK, which equates to a ratio of 2.2 and 1.9, respectively, compared to mean building height z_h . Detailed information on surface cover, building heights, their variations around the sites, and the implications for surface roughness are discussed by [Kotthaus and Grimmond \(2013\)](#). They also analyse potential impacts from the River Thames in close vicinity of the sites to the south ([Fig. 1](#)).

2.2. Data collection and processing

Three components of the surface energy balance are measured directly: net all-wave radiation and the turbulent fluxes of sensible and latent heat. The KSK site has been operational since 2008, and KSS since 2009 ([Table 1](#)). Radiometers (CNR1 & CNR4, Kipp & Zonen) provide the four constituents of Q^* , i.e. long-wave and short-wave incoming and outgoing/reflected radiation (L_{\downarrow} , L_{\uparrow} , K_{\downarrow} , K_{\uparrow}), 15 min

¹ Observed at St. James’s Park WMO station, based on the 26 years with complete data availability in the archive of the British Atmospheric Data Centre (BADC), i.e. 1981–1991 and 1997–2011.

Table 1

Instrumentation at the two sites (KSK, KSS) and the periods within the years 2008–2012 analysed in this study, specified as day of year.

	Instrument	Model	Manufacturer	2008	2009	2010	2011	2012
KSK	Sonic anemometer	CSAT3	<i>Campbell Scientific</i>	274–366	001–280	022–365	001–365	001–091
	Infrared gas analyser	Li7500	<i>LiCOR Biosciences</i>	274–366	001–280			
		Li7500A	<i>LiCOR Biosciences</i>				231–365	001–091
	Weather station	WXT510	<i>Vaisala</i>	274–366	001–365	001–365	001–069	
		WXT520	<i>Vaisala</i>				096–365	001–091
	Radiometer	CNR1	<i>Kipp & Zonen</i>	274–366	001–280			
		CNR4	<i>Kipp & Zonen</i>			264–365	001–365	001–091
Rain gauge	ARG100	<i>Campbell Scientific</i>	274–366	001–365	001–365	001–365	001–091	
Ceilometer	CL31	<i>Vaisala</i>	274–366	001–112				
KSS	Sonic anemometer	CSAT3	<i>Campbell Scientific</i>		305–365	001–365	001–365	001–084
	Infrared gas analyser	Li7500	<i>LiCOR Biosciences</i>		305–365	001–365	001–365	001–084
	Weather station	WXT510	<i>Vaisala</i>		286–356	001–365	001–365	001–084
	Radiometer	CNR1	<i>Kipp & Zonen</i>		289–356	001–365	001–365	001–084
	Rain gauge	ARG100	<i>Campbell Scientific</i>		351–365	001–365	001–365	001–091
	Ceilometer	CL31	<i>Vaisala</i>		112–365	001–365	001–365	001–091

averages are recorded. Radiation data are restricted to physically reasonable thresholds and short-wave radiation is forced to zero during night-time to correct for the instrument related night-time offset error ([Michel et al., 2008](#)).

Cloud cover was retrieved from atmospheric backscatter observed with a ceilometer (CL31, Vaisala) located near KSK (until April 2009) and then KSS (April 2009 to present). Based on the vertical atmospheric backscatter profile observed, the cloud height derived by the instrument software was used in the post-processing to determine cloud cover as a percentage. As the ceilometer raw data (8192 Hz mean pulse repetition rate, [Münkel et al., 2006](#); 15 s reporting interval) give an instantaneous profile above the sensor, the field of view is increased by using a 30 min moving window to determine the percentage of time when clouds at any height are detected (centred at each 15 s interval). The 15 s values were again averaged to 15 min intervals to coincide with the time periods of the radiation measurements.

The turbulent exchanges of latent and sensible heat are observed using the eddy covariance (EC) method. Systems at both sites consist of a CSAT3 sonic anemometer (Campbell Scientific) and a Li7500 (Li7500A) open path infrared gas analyser (LiCOR Biosciences), sampled at 10 Hz. Automatic weather stations (WXT510 and WXT520, Vaisala) provide air temperature, station pressure, horizontal wind speed and direction, as well as relative humidity, sampled at 0.2 Hz. The latter is converted to vapour pressure deficit (VPD). Tipping bucket rain gauges (ARG100, Campbell Scientific) are used to monitor precipitation; accumulated rain is recorded based on 15 min intervals. The sonic anemometer, gas analyser, rain gauge and net radiometer are connected to dataloggers (CR3000 and CR5000, Campbell Scientific). Flux calculations are performed based on 30 min block averages. All recording and data analysis is done in UTC (Universal Time Coordinated) which is local time in the winter and an hour earlier during summer (daylight savings period).

Meteorological observations from the weather stations and the rain gauges are cleaned and gap-filled ([Kotthaus and Grimmond, 2012](#)). Eddy covariance fluxes are calculated by ECPack ([van Dijk et al., 2004](#)) with a series of pre- and post-processing steps which are implemented in order to improve the quality of the results and to maximise data availability. A detailed description of the data processing procedure is presented by [Kotthaus and Grimmond \(2012\)](#). Tests comprise a new despiking approach and an automatic Identification of Micro-scale Anthropogenic Sources (IMAS, [Kotthaus and Grimmond, 2012](#)). The latter is used to filter effects of micro-scale emissions so that the calculated fluxes are representative for the local scale source area. The [Kotthaus and Grimmond \(2012\)](#) algorithm used here is improved in order to capture periods of extremely high temperatures (i.e. IMAS Type V is similar to Type II but more persistent). The updated IMAS algorithm (summarised in [Table 2](#); see [Kotthaus and Grimmond, 2012](#) for details) is applied to all data presented in the current study. Only small emission sources are present at KSK so that IMAS generally has less impact than at KSS. However, even

Table 2

Five IMAS types: (a) classification, (b) definition, and (c) detection are based on observations of sonic temperature T_{sonic} and concentrations of H_2O and CO_2 . The classification considers if there is an increase (\uparrow) or decrease (\downarrow) of the variable during an IMAS event. Statistics used in the definition and detection are calculated based on 10 s intervals: mid-range (mr_{10s} = mean of minimum and maximum) and standard deviation (std_{10s}); 1 min intervals: mid-range (mr), standard deviation (std), median (med), kurtosis (krt), and absolute deviation of the mid-range from the mean (mrm); 30 min intervals: median (med_{30}), standard deviation (std_{30}). Also, the minimum (MIN_1) and inter-quartile range (IQR_1) of mr_{10s} and the median (MED_{30}) of med are calculated over 1 min and 30 min intervals, respectively. IMAS Types I–IV are presented in Kotthaus and Grimmond (2012). Type V is included in the improved IMAS algorithm used for the current study.

IMAS	T_{sonic} [$^{\circ}\text{C}$]	H_2O [mmol m^{-3}]	CO_2 [mmol m^{-3}]
(a)	Classification		
Type I	(\uparrow)	\uparrow	\uparrow
Type II	\uparrow	\downarrow	$-$
Type III	\uparrow	\downarrow	\uparrow
Type IV	\uparrow	\downarrow	\uparrow
Type V	\uparrow	$-$	$-$
(b)	Definition		
Type I	$-$	$-$	$mrm > 0.7$ & $krt > 0.3$
Type II	$(mrm > 1$ & $krt > 3)$ or $(std > 1$ & $krt > 7)$	$-$	$-$
Type III	$krt > 1$	$mrm < -0.5$	$-$
Type IV	$(std > 0.9$ & $krt > 1)$ or $(med - MED_{30}(med)) > 1$	$mrm < -0.1$	$mrm > 5$
Type V	$(mr - med_{30}) > 0.9$ or $mrm > 2.5 std_{30}$	$-$	$-$
(c)	Detection		
Type I	$-$	$mr_{10s} > MIN_1(mr_{10s}) + IQR_1(mr_{10s})$	$-$
Type II	$mr_{10s} > MIN_1(mr_{10s}) + IQR_1(mr_{10s})$	$-$	$-$
Type III	$std_{10s} > 0.5$	$-$	$-$
Type IV	Whole 30 min period detected as IMAS		
Type V	$mr_{10s} > MIN_1(mr_{10s}) + IQR_1(mr_{10s})$ or $std_{10s} > 0.5$	$-$	$-$

at the KSS site, IMAS is mainly detected under easterly wind directions so it hardly concerns fluxes from the main wind directions (in the southwest and northeast, Kotthaus and Grimmond, 2013). After quality control, 751.2 days at KSS (1056.4 days at KSK) of sensible heat flux data are available for analysis (Table 1). More data fail quality control criteria for latent heat flux, leaving 685.2 at KSS (490.3 at KSK) days for interpretation (note that at KSK, the sonic anemometer has a much longer measurement period than the gas analyser).

Daily-accumulated energy fluxes of net all-wave radiation, sensible heat flux and latent heat flux are estimated based on median monthly diurnal patterns. Frequency distributions of the observed fluxes by time of day (not shown) reveal a slightly systematic under representation of specific hours when more observations are affected by micro-scale anthropogenic emissions. However, the overall data availability is still high, i.e. for more than 94% (82%) of the time at least twenty observations contribute to each monthly median of 30 min Q_H (Q_E) values and the number of samples never drops below 12 (10). Hence the median diurnal pattern is assumed to describe the monthly statistics sufficiently accurately such that they provide the basis for the calculation of monthly mean daily totals, rather than gap-filling individual time periods. Using the mean instead of the median leads to very similar results for Q_H (ca. 2% difference); however, indicating a sufficiently normal distribution. This difference is somewhat larger for Q_E (ca. 17%), however this represents about 5 W m^{-2} and hence is probably within the range that can be expected for the uncertainty of this flux.

Anthropogenic heat fluxes Q_F are estimated using the GreaterQf model (Iamarino et al., 2012). This quantifies building emissions (Q_{Fb}), road traffic (Q_{Ft}) and metabolism (Q_{Fm}), with:

$$Q_F = Q_{Fb} + Q_{Ft} + Q_{Fm},$$

on a regular grid with 200 m resolution. These values represent total fluxes of sensible and latent heat flux contributions. The Q_F grids are chosen based on the modelled source area (Kotthaus and Grimmond, 2013), i.e. variable in time and space, to try to ensure the Q_F values are representative of the surface volume observed by the EC method. Depending on wind direction, between two to four grid values are combined.

As anthropogenic heat fluxes from building emissions vary with air temperature (Sailor and Lu, 2004), the temperature variations observed (Oct 2008–Mar 2012, Table 1; Section 3.1, Fig. 3) were accounted for using relations determined from Iamarino et al.'s (2012) data (Fig. 2). Daily mean building anthropogenic heat flux from the GreaterQf model for the four-year period 2005–2008, was compared to air temperature at a site in central London (St. James's Park WMO station, Fig. 1a). Above a threshold temperature ($\approx 17.5\text{ }^{\circ}\text{C}$) Q_{Fb} remains effectively constant, whereas below this approximately linear functions describe the relation (Fig. 2). Because of the strong impact of human activities, the coefficients differ between weekdays (Fig. 2a) and weekends (Fig. 2b). This modelled Q_{F} indicates the order of magnitude that can be expected as direct anthropogenic energy input into the urban source volume.

Storage heat flux ΔQ_{S} was not directly observed or modelled in the current study. However, in this dense urban environment it is expected to be a significant energy balance flux when calculated as the residual of the incoming and outgoing energy terms:

$$Q_{\text{RES}} = Q^* + Q_{\text{F}} - (Q_{\text{H}} + Q_{\text{E}}).$$

Energy balance closure, which this assumes, is complicated by spatial as well as temporal variations of each of the fluxes (Offerle et al., 2005), thus adding uncertainty. However, this residual provides some useful insight into the storage heat flux. For the energy balance discussion (Section 3.3.1), it is assumed that the footprint of the radiation fluxes is representative of the local scale source area of the turbulent fluxes. According to Kotthaus and Grimmond (2013) both types of observations are mostly influenced by impervious surfaces, suggesting this approach is feasible. Their spatial analysis suggests that horizontal advection induced by channelling along the River Thames may impact the observations at KSS, reducing the sensible heat flux observed for certain wind directions. This potential energy loss would result in an overestimation of Q_{RES} .

3. Results

3.1. Meteorological conditions

The meteorological conditions observed in central London at KCL (Fig. 3, Table 1) over a period of 3.5 years provide the context for the analysis of surface energy exchange. With respect to the whole observation period, maximum (minimum) air temperature ranged from $16.9\text{ }^{\circ}\text{C}$ ($-5.4\text{ }^{\circ}\text{C}$) during winter (DJF) to $30.9\text{ }^{\circ}\text{C}$ ($7.4\text{ }^{\circ}\text{C}$) during summer (JJA). Annual rainfall was highest in 2010 (581.4 mm) compared to 2009 (525.7 mm) and 2011 (546.0 mm), respectively. The beginning of 2012 (JFM) was dry

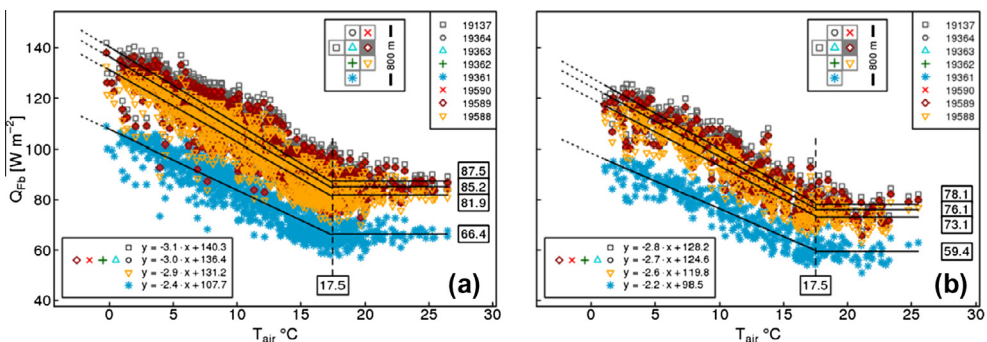


Fig. 2. Mean daily (24 h) anthropogenic heat flux from building emissions modelled with the GreaterQf model (Iamarino et al. 2012) as a function of mean daily temperature observed at St. James's Park Met Office (WMO) station (Fig. 1) for 2005–2008 for (a) weekdays and (b) weekends. Eight $200\text{ m} \times 200\text{ m}$ model grids (legend = grid ID) are selected to represent the source area of the turbulent fluxes (see Kotthaus and Grimmond 2013). (Top inset) grid locations relative to measurement sites which are both situated in the shaded grid square; (bottom inset and boxed labels) equations and coefficients to describe functions fitted to the data (solid lines); (dotted lines) indicate course for lower temperatures (as in observation period); see Section 2.2.

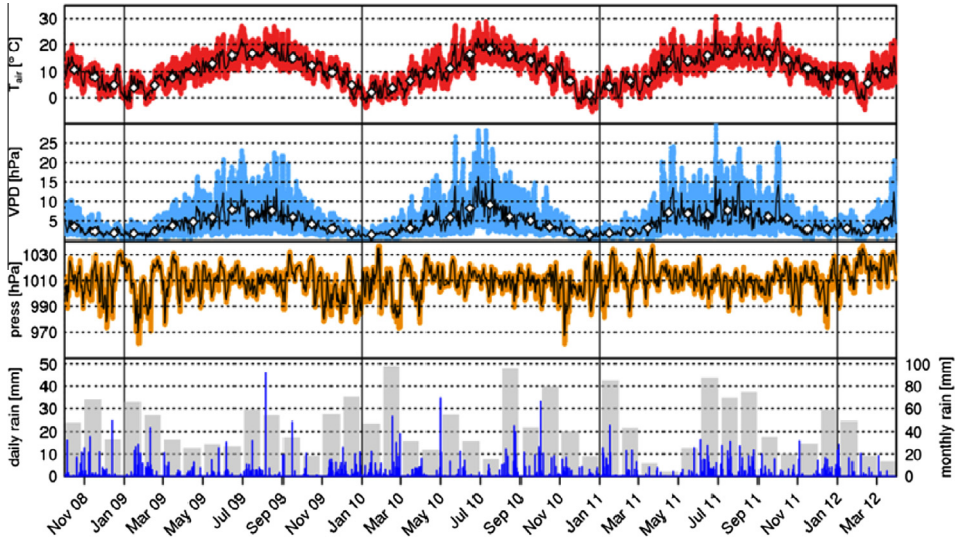


Fig. 3. Meteorological observations (after quality control) for 10/2008–03/2012, measured with a WXT510 (WXT520) weather station and ARG100 rain gauge at KSK, gap filled with KSS: air temperature, vapour pressure deficit, and station pressure as 15 min (dots), daily (solid line) and monthly averages (diamonds); daily (lines) and monthly (bars) accumulated precipitation.

with only 80.9 mm, whereas 150.0 mm rainfall fell in the last 3 months of 2008. At the monthly time scale: most rain was recorded in February and August 2010 (98.0 mm; 96.2 mm) and the least in March and April 2011 (11.6 mm; 4.0 mm). The coldest (and driest) months were January and December 2010 (2.0, 1.2 °C) while November 2011 to January 2012 was anomalously warm (11.4, 7.9, 7.7 °C, NDJ). The dry April 2011 was warmer (13.7°C) compared to April 2009 (10.9 °C) and 2010 (9.9 °C), respectively. The wind speed usually ranges from 0.2 to 6.0 m s⁻¹, occasionally reaching higher values (not shown). The overall mean wind velocity at KSS (KSK) is 3.4 m s⁻¹ (2.7 m s⁻¹).

At the synoptic scale of several days to weeks, both air temperature and humidity respond to mid-latitude high- and low-pressure systems. Passages of the latter show up clearly in the observed station pressure (Fig. 3). Persistent high pressure is usually associated with clear sky conditions, enabling long-wave radiative cooling at night and short-wave radiative heating during the day. Due to low solar elevation angles, the effect of heat loss dominates in winter so that air temperature decreases considerably when high pressure persists for several days (e.g. 26/12/2008–10/01/2009). Naturally, little precipitation is recorded during these times, which contributes to the relatively lower levels of humidity (e.g. 01/03–18/03/2010).

3.2. Radiation components

Radiative energy is generally the most important source in the surface energy balance. All four components of the net-all wave radiation are observed at KCL Strand (Fig. 1b): a combined time series of measurements at the two sites (KSK: 10/2008–09/2009; KSS: 11/2009–03/2012; CNR1, Table 1) illustrates their variability (Fig. 4).

3.2.1. Short-wave radiation

At the central London sites, daytime maxima of incoming short-wave radiation (K_i) range from about 200 W m⁻² in winter to 1000 W m⁻² in summer. As expected there is little inter-annual variation. Surface influence is evident in observations of reflected short-wave radiation (K_r). While daily maxima usually range between 50 W m⁻² (winter) and 120 W m⁻² (summer), some extreme values are observed at both sites (Fig. 4). They occur more frequently at KSK (2008 & 2009) where many of them exceed 150 W m⁻². Fewer extremes are seen at KSS (mainly in May and September

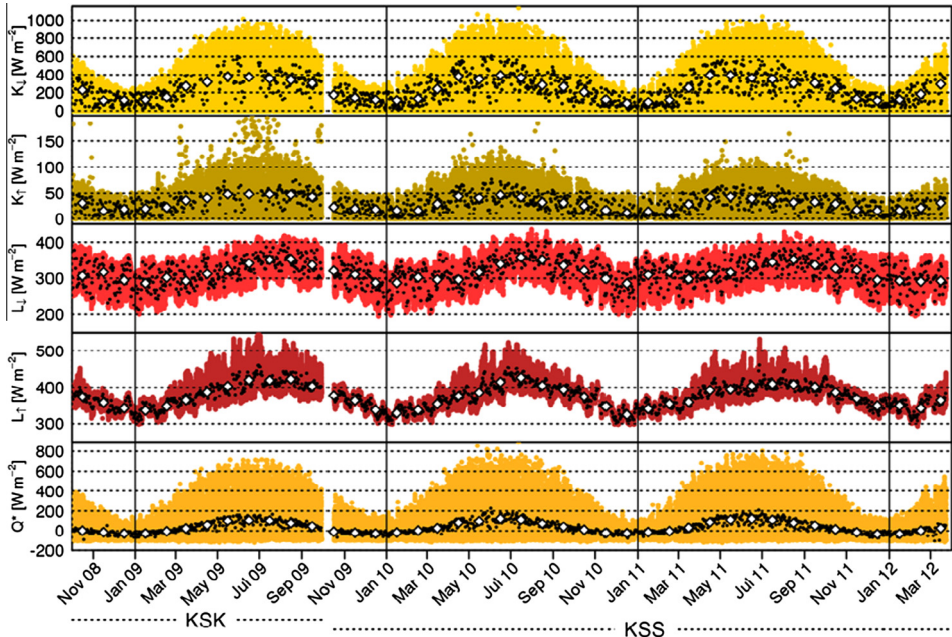


Fig. 4. Observations of the CNR1 net radiometer (after quality control) at KSK (10/2008–09/2009) and KSS (10/2009–03/2012): net all-wave radiation Q^* is the sum of incoming (\downarrow) and outgoing (\uparrow) long- (L) and short-wave (K) radiation, averages: 15 min (coloured dots), daily (K : daytime, L & Q^* : 24 h, black dots) and monthly (white diamonds). Data gap in October 2009 due to maintenance.

2010 & 2011). These ‘outliers’ are caused by specular reflections at surfaces of high reflectivity in the radiometer’s source area (Kotthaus and Grimmond, 2013). Kotthaus and Grimmond (2013) investigate the impact of surface heterogeneity and cloud cover on observations of surface albedo. They conclude that the lower bulk surface albedo of 0.11 at KSS (compared to 0.14 at KSK) is more representative of the local-scale.

3.2.2. Long-wave radiation

Variations of incoming long-wave radiation (L_{\downarrow}) can be expressed as a function of near surface atmospheric conditions (temperature and humidity) and presence of (low) clouds (Flerchinger et al., 2009). The annual cycle of the observed down-welling thermal radiance (Fig. 4) is characterised by larger energy fluxes during warm and dry times of the year (Fig. 3). At the two central London sites, daily maxima of L_{\downarrow} range from about 350 W m^{-2} in winter to 430 W m^{-2} in summer. Diurnal patterns under clear sky conditions are mostly governed by diurnal temperature variations, while long-wave radiation increases during overcast conditions. In the winter, colder air temperatures often coincide with clear sky conditions. Relatively warm autumn (or winter) periods (e.g. Nov 2011) are associated with overcast conditions that reduce radiative cooling during the night. Accordingly, the lowest monthly mean L_{\downarrow} was observed in December 2010 (285.9 W m^{-2}), the coldest month in the observation period (Section 3.1) and the coldest month on record for the whole UK (national records since 1910, MetOffice 2013).

While incoming long-wave radiation exhibits fairly strong variability throughout the year as a response to the water content of the atmosphere, its outgoing counterpart is characterised by differing behaviour between warm and cold months (Fig. 4). Outgoing long-wave radiation (L_{\uparrow}) is directly related to the skin temperature of the urban surface, hence depends on the amount of total incoming radiative energy $Q_{\downarrow} = K_{\downarrow} + L_{\downarrow}$ (in addition to convection or conduction processes) and the three-dimensional structure of the urban surface. The latter enables multiple reflections of incoming

radiation (both, short- and long-wave) which increases energy absorption by the urban canopy. However, it also is responsible for the formation of complex shadow patterns, reducing the fraction of the complete three-dimensional surface that receives direct solar insolation, and hence diminishing the surface temperature in certain areas of the canopy. This explains the variations of the diurnal range of L_i over the course of the year, with larger scatter seen from April to September (Fig. 4). During winter the urban fabric does not warm up as much, rather it stays close to the near surface air temperature whose pattern can then be recognised in the time series of outgoing long-wave radiation (compare T_{air} in Fig. 3 and L_i in Fig. 4, e.g. Feb 2012).

The dependence of long-wave radiation fluxes on cloud cover was examined separately for day and night-time (Fig. 5). In order to account for variations of day-length, medians by cloud cover percentage are presented as a function of solar elevation angle during daytime (Fig. 5e) and as a function of standardised night-time, i.e. night-time normalised by night-length (Fig. 5a–c). Ceilometer cloud cover percentages were binned into 12 classes. Their frequencies (presented as total duration in days) reveals that clear-sky (cloud cover = 0%) and overcast conditions (cloud cover = 100%) depict the most common classes. The high frequencies at both ends of the distribution, compared to adjacent classes (e.g. compare = 100% to $90\% \leq$ cloud cover < 100%), were confirmed by comparison to cloud cover derived from diffuse radiation measurements (not shown). The distribution is probably explained by persistence of meteorological conditions that favour overcast and clear-sky conditions for longer periods (up to several days), while partly cloudy skies are associated with more variable atmospheric conditions.

Clouds enhance incoming long-wave radiation, which is particularly important during the night when this is the only incoming radiative flux (Fig. 5a). When night-time values of incoming long-wave radiation were normalised by the sunset value (termed here ‘sunset fraction’, SSF), a slight increase (decrease) is evident over the course of the night for overcast (clear sky) conditions (not shown). This is probably explained by the different cooling rates of the atmospheric column and the associated

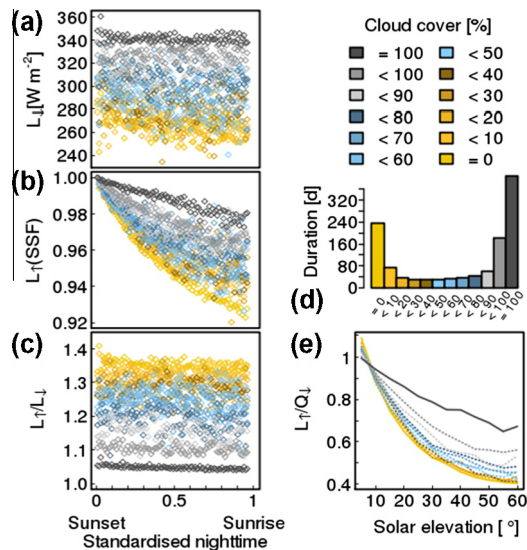


Fig. 5. Long-wave radiation fluxes stratified by cloud cover [%] separately for (a–c) night (by standardised night-time) and (e) day (by solar elevation angle); (d) Accumulated duration of detected cloud cover in days [d] in 10% bins (interval definition: lower limit \leq cloud cover < upper limit; except for clear sky (totally overcast) conditions with cloud cover = 0% (=100%)). Only those periods are included when measurements of all relevant radiation components are available. (a) Incoming long-wave radiation, (b) outgoing long-wave radiation normalised by the value observed at sunset: sunset fraction SSF, (c) ratio of outgoing and incoming long-wave radiation, and (e) outgoing long-wave radiation normalised by total incoming radiation Q_i . Observations (CNRI) are from KSK (Oct 2008–2009) and KSS (Nov 2009–Mar 2012).

changes in vapour pressure. In terms of absolute values, no apparent impact of cloud cover can be identified in night-time outgoing long-wave radiation. However, the SSF of L_{\uparrow} clearly illustrate that cooling rates of the urban surface decrease with increasing cloud cover (Fig. 5b), i.e. over the course of a night with 100% (0%) cloud cover L_{\uparrow} decreases by an average of 2% (7%). This is probably explained by the fact that clear sky nights often follow a day with low cloud cover so that more energy was stored in the canopy and surface temperatures tend to be higher. However, a small fraction of the outgoing long-wave radiation is attributed to reflected and re-emitted L_{\downarrow} , introducing a secondary dependence to cloud cover. The amount of reflected L_{\uparrow} is particularly important where materials with low emissivity are present. The night-time radiation balance (Fig. 5c) reveals that up to 35% more energy is observed to leave the surface via radiative processes than is received ($L_{\uparrow} \approx 1.35 L_{\downarrow}$ for clear skies) whereas the long-wave fluxes are close to equilibrium for overcast sky conditions.

During daytime, when short-wave radiative input significantly increases the total incoming radiation flux, the median ratio of outgoing long-wave radiation to all-wave radiative input ($L_{\uparrow}/Q_{\downarrow}$) is lower than unity (Fig. 5d). K_{\downarrow} accounts for the pronounced variation with solar elevation angle during daytime with minimal values of the median $L_{\uparrow}/Q_{\downarrow}$ fraction at maximum irradiance (for maximum sun elevation and clear sky conditions) of about 0.4. Hence, for a certain solar elevation angle during daytime, the normalised outgoing long-wave radiation $L_{\uparrow}/Q_{\downarrow}$ increases with higher cloud cover.

Net all-wave radiation Q^* (Fig. 4) combines all four components of the radiation balance and hence incorporates all their dependencies on sun elevation, cloud cover and surface characteristics. Daily maximum values range from about 150 W m^{-2} in winter to about 700 W m^{-2} in summer. The overall slightly lower values of the radiation budget before November 2009 are explained by KSK's higher surface albedo (Kotthaus and Grimmond, 2013). During winter months, radiative cooling exceeds the gain from solar input so that monthly median Q^* becomes negative.

3.3. Temporal variations of surface energy exchange

Net all-wave radiation Q^* , sensible heat flux Q_H and latent heat flux Q_E all exhibit a pronounced diurnal cycle throughout the year (Fig. 6). In addition to their monthly median diurnal patterns (lines, Fig. 6), accumulated energy fluxes (also for day- and night-time) are presented (bars, Fig. 6). Diurnal and seasonal patterns seen in the net all-wave radiation are formed by a combination of the processes affecting its components (Section 3.2). Nocturnal radiative cooling (negative Q^*) is generally stronger from March till October when more heat is stored within the urban canopy and surface temperatures are higher (compare Figs. 3 and 6). However, due to reduced daylight periods in winter, more energy is lost by the surface volume during the night than gained during the few hours of incoming solar radiation. The monthly 24 h - radiation budget is negative from November to January. During these months, total upward energy flux during the night ($1.2\text{--}3.2 \text{ MJ d}^{-1} \text{ m}^{-2}$) exceeds the energy gained during the short days ($0.2\text{--}1 \text{ MJ d}^{-1} \text{ m}^{-2}$). Particularly large total night-time radiation flux ($>3 \text{ MJ d}^{-1} \text{ m}^{-2}$) also occurred in spring and autumn (Apr & Sep 2011, Mar 2012). However, these months had large energy daytime gains associated with predominantly clear sky conditions, high air temperatures, low humidity and small precipitation amounts (Fig. 3). Positive monthly median net-all wave radiation from March to September provides energy for turbulent fluxes and conduction into the surface. The largest gain of radiative energy by the surface is between April and July, ranging between 3.3 and $11.2 \text{ MJ d}^{-1} \text{ m}^{-2}$. February and November mark the transition periods with very small total fluxes in either direction.

Sensible heat flux Q_H is largest from April to September (Fig. 6) when its monthly median diurnal maxima often exceed 200 W m^{-2} and accumulated daytime upward energy transport (about $6.7\text{--}9.8 \text{ MJ d}^{-1} \text{ m}^{-2}$) accounts for most of the 24 h - total flux (about $9.0\text{--}12.2 \text{ MJ d}^{-1} \text{ m}^{-2}$). During colder months when net all-wave radiation provides less energy into the system, daytime sensible heat fluxes are considerably lower. However, even at these times sensible heat flux continues to provide significant energy transport away from the surface into the urban boundary layer, with median diurnal maxima of at least 100 W m^{-2} (December and January). This suggests that strong anthropogenic energy sources are located in the study area. A combination of anthropogenic heat flux and a large heat storage capacity of the urban canopy could further explain the constant night-time upward transport of sensible heat at the central London site (Fig. 6). As found for other dense urban environments

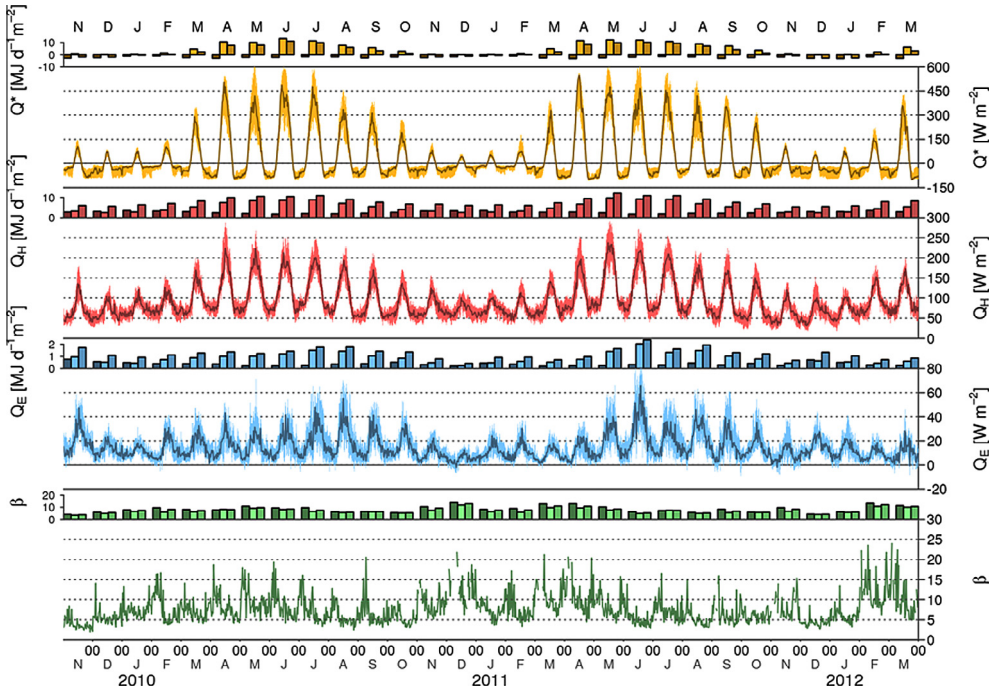


Fig. 6. Monthly energy fluxes at KSS (11/2009–03/2012): (vertical bars) accumulated energy flux for (left) night, (middle) day, and (right) total 24 h; (solid line) median diurnal patterns with inter-quartile range (shading) of net all-wave radiation Q^* , sensible heat flux Q_H , and latent heat flux Q_E . Lowest panel (solid line) is the Bowen ratio (β —ratio of the monthly median diurnal Q_H/Q_E fluxes); (vertical bars) mean β separated into (left) night-time, (middle) daytime, and (right) total 24 h. β only calculated for times with considerable latent heat flux, i.e. $|Q_E| > 3 \text{ W m}^{-2}$.

(e.g. Mexico City, Velasco et al., 2005), Q_H remains positive throughout the night and is observed to almost exclusively be responsible for energy transport away from the surface (only 0.5% of all nocturnal Q_H estimates are negative).

Monthly median nocturnal Q_H fluxes have lower magnitudes during winter (around 50 W m^{-2}) than summer (around 80 W m^{-2}), but these still are larger flux values than found in comparable studies such as for Marseille (Grimmond et al., 2004) or Basel (Christen and Vogt, 2004). Due to the short day-length in the cold season, day- and night-time totals are comparable in November and February. In December and January, nocturnal sensible heat flux even exceeds daytime totals. Thus, the monthly 24 h – sensible heat flux never falls below $5.3 \text{ MJ d}^{-1} \text{ m}^{-2}$ (Nov 2011).

A comparison between the monthly median incoming radiative energy and the turbulent sensible heat transport indicates a large anthropogenic component in the surface energy balance. In general, total monthly turbulent sensible heat flux exceeds radiative input (by up to $8.5 \text{ MJ d}^{-1} \text{ m}^{-2}$, Jan 2012) and only for 1 month in the observation period (Jun 2010) is it less than the 24 h – radiation budget (by $0.8 \text{ MJ d}^{-1} \text{ m}^{-2}$). Some of this discrepancy might be explained by the differing source areas of the two energy flux estimates. However, especially during winter, when both fluxes characterise net energy loss by the urban surface volume, considerable energy would need to originate from alternative sources. Under the assumption of a balanced storage heat flux (over the course of 24 h) and negligible horizontal advection, this is most likely associated with anthropogenic activities (Section 3.3.1). Note, there is evidence that the KSS fluxes might be affected by advective fluxes under some flow conditions (Kotthaus and Grimmond, 2013) which adds uncertainty to the residual term. However, those situations are associated with a decrease in sensible heat flux and hence a reduction in the discrepancy between radiation and turbulent fluxes.

The turbulent latent heat flux Q_E observed at KSS (Fig. 6) exhibits a diurnal pattern that is presumably driven by the course of available energy as the moisture availability in central London can be assumed to not vary systematically over a 24 h period. The surface cover is dominated by impervious surfaces with little vegetation (Kotthaus and Grimmond, 2013). Hence, seasonal phenological variations (which might be strong enough to contribute slightly to enhanced evaporation from late spring to early autumn) would be difficult to detect in the local scale measurements. The River Thames to the south and southwest of the site was not identified as a significant source for evaporation and the spatial morphology may impede the measurement of large local-scale EC evaporation fluxes from this source (Kotthaus and Grimmond, 2013). Monthly total latent heat flux ranges between approximately $0.4\text{--}2.4 \text{ MJ d}^{-1} \text{ m}^{-2}$. As for the sensible heat flux, nocturnal fluxes are larger during warmer months, but with generally small magnitudes ($<20 \text{ W m}^{-2}$). Occasionally, the monthly median latent heat flux is very close to zero or even negative. This could correspond to downward moisture transport. However, given the uncertainty of these measurements, values of such small magnitude should be interpreted with caution.

Precipitation seems to be the most likely driving factor for temporal variations in the evaporative flux. Months with high amounts of accumulated rainfall (Section 3.1, Fig. 3) tend to have increased Q_E and a corresponding lower Bowen ratio β (here calculated as monthly median diurnal Q_H over Q_E). The Bowen ratio (Fig. 6) is persistently dominated by the sensible heat flux. Monthly median hourly values mostly range between five and ten (solid line in lower panel of Fig. 6). In comparison to previous urban surface flux observations, these Bowen ratio values are at the higher end. Most flux sites in European cities have more vegetation in the measurement footprint. At these sites, Bowen ratio values are below 2 during summer and up to about 5 when vegetation effects are limited during winter (Goldbach and Kuttler, 2012, their Table 1) or the vegetation fraction in the source area of the flux site is extremely small (Marseille, France; Grimmond et al., 2004). An example for observations at a vegetation-free site is presented by Christen and Vogt (2004) who measure a Bowen ratio of 6 at the top of a canyon in Basel in the summer. On a monthly basis, the mean Bowen ratio is slightly larger during the night. However, generally it is quite independent of the averaging period (compare 24 h, nocturnal and daytime bars in lower panel of Fig. 6).

3.3.1. Atmospheric stability

The persistently strong net upward motion of warm air can be expected to have an influence on the atmospheric boundary layer in central London with important implications for air quality and larger scale meteorological processes. The observed positive nocturnal sensible heat fluxes impact the atmospheric stability, which is represented by the stability parameter $\zeta = z'/L$, where L is the Obukhov length and z' the effective height ($z' = z_m - z_d$, the difference between measurement height z_m and zero-plane displacement height z_d). The relative frequency of stability conditions by time of day (Fig. 7), divided into four stability classes (extremely unstable: $\zeta < -0.5$, unstable: $-0.5 \leq \zeta < -0.1$, neutral: $-0.1 \leq \zeta < 0.1$, and stable: $0.1 \leq \zeta$) and for warmer periods with higher sensible heat flux (Apr–Sep) and colder periods with lower sensible heat flux (Oct–Mar), shows that, overall, only 0.5% of all observations are classified as stable. This could be explained by the predominantly high turbulent sensible heat fluxes (no minimum threshold has been applied for Q_H during the calculations of ζ). In addition to the strong upward motion maintained by the dense urban environment, the high roughness of the urban canopy (Kotthaus and Grimmond, 2013) is reflected in the stability parameter. While it is probably the significant buoyancy that inhibits stable stratification, the magnitude of the friction velocity u^* (not shown) seems to determine which of the remaining three stability classes is applicable.

At KSK (Fig. 7a), local stability is neutral more than half the time in both parts of the year and about 15% of the time very unstable. The diurnal pattern of unstable conditions varies little with season but daytime frequencies increase in Apr–Sep at the expense of neutral conditions which become more likely at night. At KSS, the variations with season appear a bit more complex (Fig. 7b). In the colder months (Oct–Mar) the probability of neutral and unstable conditions is similar with both around 40–50% over the course of the day. Diurnal variations favouring neutral conditions during the night compared to the day are hardly detectable. However, during the warmer months (Apr–Sep) neutral conditions make up less than 40% until late afternoon (1600 UTC) and become more likely (even

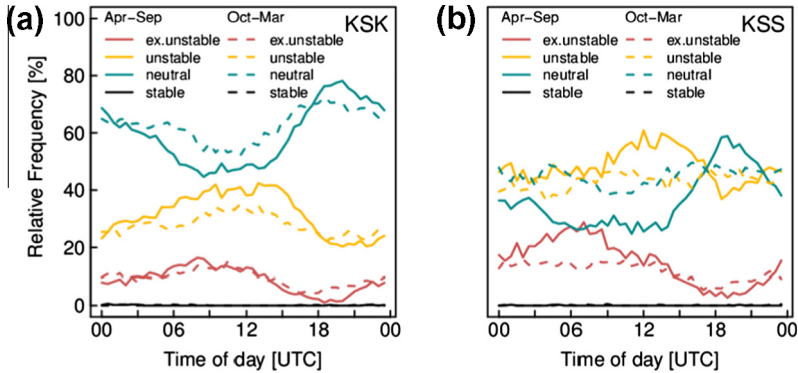


Fig. 7. Relative frequency of stability conditions by seasons or strength of sensible heat flux: spring/summer (Apr–Sep, stronger) and autumn/ winter (Oct–Mar, weaker) for (a) KSK and (b) KSS. See text for stability definitions.

exceeding 50%) in the evening hours. Very unstable conditions are more frequently observed in the early morning hours and unstable conditions during daytime. Overall, about a third of the observations at KSS are classified as neutral.

Presumably, observations at the lower KSK site are more influenced by the immediate surroundings than those at KSS (Kotthaus and Grimmond, 2013). A combination of variations in radiative energy input and increased roughness effects explains the increased probability of neutral local stability at this lower site. The observations at KSS (Fig. 7b) are a result of surface atmosphere exchanges over a larger, local scale area where storage heat flux and anthropogenic heat flux play a major role in the surface energy balance (Section 3.3.1). These maintain buoyant heat fluxes and hence make neutral stratification less likely.

At both sites during Apr–Sep neutral conditions show their peak frequency around 2000 UTC. The evening peak of neutral conditions is more pronounced at KSS, where this reaches 60% at 1800 UTC but drops back to 40% at midnight. These diurnal variations appear to be associated with the diurnal patterns of Q_{H+} and u^* relative to each other (not shown). Especially during summer months, friction velocity remains high in the evening hours and decreases to night-time magnitudes later than the turbulent heat flux, causing peak ζ -values during that time of day. The diurnal pattern of the friction velocity is less pronounced during winter. These flow patterns may be influenced by horizontal advection induced by the River Thames (Kotthaus and Grimmond, 2013).

3.3.2. Energy partitioning

The timing of turbulent energy transport with respect to solar noon is evaluated by normalising the median conditions (based on all data) by their respective maxima (Fig. 8). This climatological analysis confirms that both turbulent fluxes start rising in the early morning hours and reach their maxima later than the radiative fluxes because of the uptake of energy by the storage heat flux. In addition to this well-known time lag between radiative input and turbulent surface energy exchange, a shift between the sensible heat flux and the latent heat flux is observed. The normalised estimates show that evaporation is relatively higher in the afternoon compared to the morning hours, which is probably explained by the rising water vapour pressure deficit. The relatively stronger evaporation after solar noon results in a pattern of decreasing Bowen ratio (diamonds in Fig. 8) from ~ 7.4 to ~ 5.5 . The slightly decreasing relative importance of sensible heat leads to a robust estimate of daytime Bowen ratio of 6.4 for the central London site (6.5 for hours when $K_{\downarrow} > 0 \text{ W m}^{-2}$; 6.4 for hours when $Q^* > 0 \text{ W m}^{-2}$ and a period of 2 or 4 h around solar noon). The independence of the chosen time interval suggests that, due to the diurnal variation of energy partitioning, no uncertainty should arise from differing definitions of the time period of interest when comparing the average Bowen ratio estimate to those found in other studies (Goldbach and Kuttler, 2012), which often do not have consistent daytime periods applied for the calculation of β .

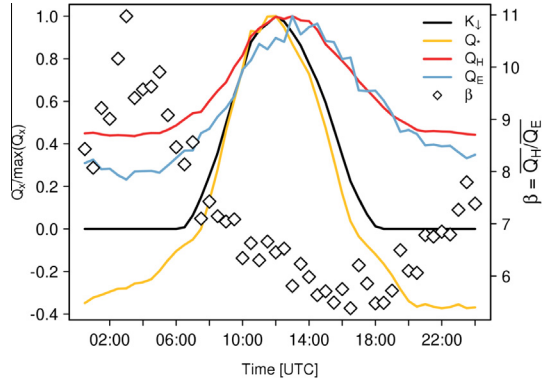


Fig. 8. Median diurnal pattern of energy fluxes Q_x at KSS, normalised by respective maximum $\max(Q_x)$: net all-wave radiation Q^* , shortwave incoming radiation K_i , and turbulent fluxes of sensible heat Q_H and latent heat Q_E . Bowen ratio β (diamonds) calculated from the median diurnal patterns of sensible and latent heat flux (restricted to $|Q_E| > 3 \text{ W m}^{-2}$).

On a monthly time scale, times with high accumulated precipitation seem to slightly favour the evaporation flux, leading to smaller Bowen ratio values (compare Figs. 3 and 6). However, due to the overall very weak evaporation fluxes, the potential link between rainfall and energy partitioning is not always clearly evident in the magnitude of Q_E . Rather, available energy appears to be the dominant driving factor. At shorter time intervals again, it can be illustrated that more energy is used for evaporation directly after rain (see the frequency distribution of the Bowen ratio relative to the time since rainfall was recorded; Fig. 9; KSS). Due to quality control restrictions (Kotthaus and Grimmond, 2012) no observations are available during rainfall and the subsequent 30 min period. In the periods 1–6 h after rain, the Bowen ratio is most frequently between 1–2.5 and for some periods within the first 2–3 h Q_E is larger than Q_H ($\beta < 1$). With increasing time after rainfall, small Bowen ratio values become less likely and slightly higher values (around 3) have the highest probability until about 12 h post-event. About 8–9 h after rainfall, Bowen ratio values of greater than 10 are more probable. While evaporation is important immediately following precipitation, the sensible heat flux quickly regains its dominance. As the locally weighted regression (Lowess) and the median curve show (Fig. 9), the energy used by Q_E decreases rapidly in the first 12 h and then the energy partitioning behaves more similarly. In some cases, such as when the overall fluxes (especially the solar input) are low, water might remain on the surface for longer. However, analysis shows that after ~12–18 h most

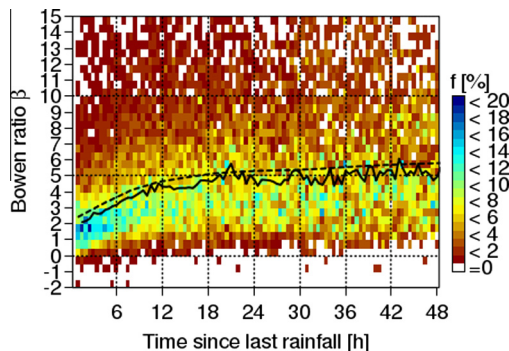


Fig. 9. Frequency distribution (frequency f [%]) of Bowen ratio β (calculated for times with considerable latent heat flux, i.e. $|Q_E| > 3 \text{ W m}^{-2}$) by time since last rainfall. Statistics (excluding $\beta > 25$, i.e. 2% of all available Bowen ratio values): locally weighted polynomial regression using Lowess filter with a smoother span of $1/5$ (dashed line) and median Bowen ratio by time since rainfall (solid line). Only Bowen ratios $\beta < 15$ and times of up to 48 h after rainfall are shown.

precipitation events no longer exert control over the energy partitioning between the turbulent fluxes of latent and sensible heat. Since the site is located in a dense urban setting where impervious surfaces dominate the land cover (Kotthaus and Grimmond, 2013), efficient surface runoff is likely responsible for this comparatively short time interval. At other sites with more bare soil or vegetation fractions, rain events can influence the energy balance over several days (e.g. Ward et al., 2013).

3.4. Monthly surface energy balance

To analyse inter-monthly variations, total fluxes measured (methodology described in Section 2.2) for the 3.5-year period are considered (Fig. 10). The energy gain and loss by the urban surface volume (positive and negative bars in Fig. 10) are shown with the anthropogenic heat flux (Q_F) derived using the GreaterQf model (Iamarino et al. 2012; Section 2.2). As suggested in the discussion of sensible heat flux estimates (Section 3.3), anthropogenic heat flux plays a major role in the surface energy balance of the study area. Monthly total model estimates selected to represent the footprint of the turbulent fluxes (Section 2.2; Kotthaus and Grimmond 2013) range between $8.6 \text{ MJ d}^{-1} \text{ m}^{-2}$ (Aug 2009) and $12.4 \text{ MJ d}^{-1} \text{ m}^{-2}$ (Dec 2010), with building emissions contributing the majority of energy. During winter, energy input appears to be governed by anthropogenic impacts while net radiative input reaches similar magnitudes as Q_F during summer. Only in June and July (and May 2011) does the energy gained by net radiation become more important than that from anthropogenic emissions. Although these data do not permit a detailed analysis of the relation between Q^* and Q_F , the combination of the two fluxes provides qualitatively reasonable patterns. While maximum radiative input occurs around June, anthropogenic impact becomes minimal from June to October due to its dependence on air temperatures (Fig. 2; Iamarino et al., 2012). Anthropogenic heat flux reaches a maximum in December and January, when radiation has a negative effect on the surface energy budget.

As discussed, both turbulent fluxes generally transport energy away from the surface (Section 3.3). Whereas Q_H has a very pronounced seasonal variability, Q_E responds strongly to moisture availability from precipitation (Section 3.3.2). Kotthaus and Grimmond (2013) investigate the effects of source area characteristics on both radiative and turbulent energy fluxes at the two nearby sites, explaining that turbulent fluxes observed at KSK (Oct 2008–2009 selected for Fig. 10) are smaller (on average by 40%) than at KSS (Nov 2009–Mar 2012) because of differences in the flow conditions observed at the two heights. At both, the overall monthly energy loss (negative bars in Fig. 10) corresponds well to the pattern of available energy (positive bars in Fig. 10). As the sum of radiative and anthropogenic input is highest in late spring/early summer strongest turbulent fluxes are observed at this time of the year.

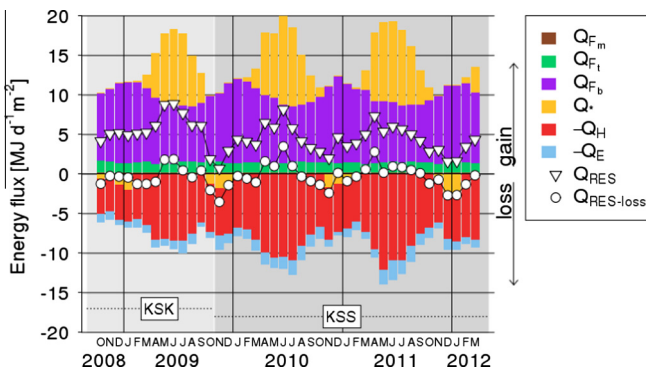


Fig. 10. Mean daily energy fluxes by month: modelled anthropogenic heat flux (metabolism Q_{Fm} , road traffic Q_{Fi} , and building emissions Q_{Fb}), and observed net all-wave radiation (Q^*), sensible heat flux (Q_H), and latent heat flux (Q_E) at KSK (10/2008–10/2009; only 5 days of observations available for 10/2009) and KSS (11/2009–03/2012). Residual (Q_{RES}) assumes energy balance closure (EBC) by month, and $Q_{RES-loss}$ with EBC assuming an underestimation of the turbulent fluxes by 20% at KSS (48% at KSK accordingly) and overestimation of the anthropogenic heat flux by 26%. Positive (negative) fluxes indicate energy gain (loss) by the surface volume.

In general, similar monthly patterns are found for negative and positive monthly totals in all years. Quantitatively, the comparison suggests that high sensible heat flux observations, including the explicit night-time contributions discussed (Section 3.3), are physically reasonable for this dense urban environment. Still, both much larger and smaller Q_H could occur. From GreaterQf model results, anthropogenic heat emissions could be larger than the sensible heat fluxes observed with the EC systems. Horizontal advection may cause reduced fluxes for certain wind direction conditions (Kotthaus and Grimmond, 2013). Thus the temporal variability is critical and long-term quantification may be misleading in the context of the overall energy balance analysis (Fig. 10).

The daily average (24 h mean) anthropogenic heat flux around the sites ranges from $\sim 73 \text{ W m}^{-2}$ (river dominated model grid in Jul 2010) to 159 W m^{-2} (impervious dominated model grid in Dec 2010). These values are high compared to those estimated for other central city areas (around 20 W m^{-2} in Basel, Christen and Vogt, 2004; up to 75 W m^{-2} in Marseille during summer, Grimmond et al., 2004; about 85 W m^{-2} in Singapore, Quah and Roth, 2011). Daily average anthropogenic heat fluxes from building emissions (GreaterQf model) are from 64 to 131 W m^{-2} whereas the building scale heat flux observations (Kotthaus and Grimmond, 2012) at the KSS site were $\sim 70 \text{ W m}^{-2}$ for sensible heat flux and 7 W m^{-2} for the latent heat. This suggests that the derived building emissions (Fig. 2) may be too high. Anthropogenic heat flux estimates are extremely scale-dependent (e.g. Kotthaus and Grimmond, 2012; Lindberg et al., 2013) so spatial (mis)alignment of the modelled fluxes to the source area of the turbulent fluxes (Section 2.2, Fig. 2) will introduce uncertainties. Despite these uncertainties, the large observed Q_H can only be maintained by anthropogenic heat sources which exceed the radiation balance in terms of providing energy to the surface nearly all year round.

Assuming energy balance closure, the residual flux Q_{RES} (Section 2.2) includes the storage heat and all the uncertainties of the measured and modelled energy balance components. A first estimate suggests the residual Q_{RES} could exceed $8 \text{ MJ d}^{-1} \text{ m}^{-2}$ in some months (triangles, Fig. 10), with highest values when energy gain is largest (mean for Apr–Aug: $Q_H + Q_E$ is $9.3 \text{ MJ d}^{-1} \text{ m}^{-2}$ [KSK 2009] or $12.0 \text{ MJ d}^{-1} \text{ m}^{-2}$ [KSS 2010–2011] and $Q^* + Q_F$ is $16.8 \text{ MJ d}^{-1} \text{ m}^{-2}$ [KSK] or $18.0 \text{ MJ d}^{-1} \text{ m}^{-2}$ [KSS]) and the minima in winter months with some large outgoing fluxes (Q_{RES} is $0.7 \text{ MJ d}^{-1} \text{ m}^{-2}$ in Nov 2009 due to high Q_E and $1.6 \text{ MJ d}^{-1} \text{ m}^{-2}$ in both Dec 2011 and Jan 2012). Although Q_{RES} remains positive suggesting a net warming, the seasonal pattern seems appropriate. However, these results include any errors (e.g. spatial mismatch of source areas, contributions of horizontal advection, and differences arising from combining observed and estimated data) so further examination of Q_{RES} is warranted.

The results suggest that some outgoing energy is not accounted for, energy input may be over-estimated and/or energy may be double counted. In terms of energy input, the net all wave-radiation may be slightly underestimated if the source areas of the radiometers are biased towards roof surfaces (especially at KSK; Kotthaus and Grimmond, 2013). As noted above, the modelled anthropogenic heat flux may be over-estimated due to potential spatio-temporal mismatch with the observations and/or due to the fact that some of it being already accounted for in the long-wave radiation balance and the turbulent fluxes observed. Obviously, some error is attributed to the modelled Q_f data from the GreaterQf model (Iamarino et al., 2012) itself. The latter however is still very difficult to quantify. EC fluxes do not always capture the full turbulent energy transported (e.g. Culf et al. 2004), as widely discussed in the context of the energy balance closure (Foken, 2008). Further, single tower flux sites are not suitable to quantify the complex issue of horizontal advection (Spronken-Smith et al., 2006). As suggested by Kotthaus and Grimmond (2013) horizontal advection induced by the River Thames may cause reduced sensible heat fluxes observed at KSS under some conditions. A second estimate assuming a 20% underestimation of the EC fluxes (e.g. Hollinger and Richardson, 2005; Dragoni et al., 2007) at KSS ($\sim 50\%$ at KSK accordingly, on average Q_H at KSK is $\sim 60\%$ of that at KSS, Kotthaus and Grimmond, 2013), and an over-estimation of Q_f by 26% (dots, Fig. 10) causes the mean annual residual to be zero.

The storage heat flux ΔQ_s , which is part of Q_{RES} , is expected to be close to zero at time scales of a day or a year but to have small monthly gains in summer and losses in winter as the urban fabric heats up and cools down. The residual flux does have the expected seasonal cycle. Anthropogenic sources are likely to affect the size of the actual storage term (Grimmond et al., 1991). It is closely related

to radiative energy which is absorbed by the surface fabric of the canyon walls and changes with solar elevation angle and surface geometry (Moriwaki and Kanda, 2004).

4. Conclusions

The dataset of observed energy exchanges in the CBD of London for a 3.5 year period discussed in this paper provides new information both with respect to urban zone (dense city centre) and seasonality (multi-year observations) for two sets of instruments in proximity. From analysis of these data the following conclusions are drawn.

At night, up to 35% more energy leaves the urban surface than is received via long-wave radiation under clear sky conditions. With increasing cloud cover this percentage decreases, so that for an overcast sky L_{\uparrow} and L_{\downarrow} are nearly equal. Cloud cover diminishes nocturnal cooling rates of the urban surface, so that outgoing long-wave radiation decreases by only 2% over the course of a night for overcast conditions compared to 7% for clear nights. During daytime, outgoing long-wave radiation drops to 40% of the total incoming radiative energy under clear sky conditions, remaining higher for overcast periods (about 70%). Although clouds play a similar role in all environments, knowledge of the impact to long-wave radiation is important because of the significant trapping of the latter in cities, which directly impacts the storage heat and sensible heat fluxes.

Sensible heat fluxes are positive all year round, even at night, sustained by a combination of storage and anthropogenic heat fluxes. Monthly median nocturnal fluxes ($50\text{--}100\text{ W m}^{-2}$) are amongst the highest observed in cities to date but are not unexpected given the building densities and activities in this central city area. The strong positive Q_H inhibits stable atmospheric stratification, which rarely occurs. However, the resulting stability classification is determined predominantly by the diurnal pattern of friction velocity over the rough urban surface. Neutral stratification (about a third of time at KSS) has peak frequencies in the early evening associated with the diurnal cycles of momentum and sensible heat fluxes.

Turbulent latent heat fluxes are very small, with variations in phenology not detectable due to the small surface vegetation fraction. Rather, variations are controlled (beyond the available energy) by rainfall. The Bowen ratio immediately following rainfall is depressed. Values of between 1 and 2.5 dominate for a period 1–6 h after the event. Thereafter the ratio increases as impervious surfaces remove surface water efficiently. The effect of most precipitation events is limited to a period between 12 and 18 h after the rain has stopped. The Bowen ratio is mostly larger than one (mean $\beta = 6.4$ at KSS) and decreases throughout the day.

Turbulent sensible heat flux systematically exceeds the input from net all-wave radiation. Analysis at the monthly time scale demonstrates these high Q_H fluxes are likely maintained by anthropogenic heat fluxes which may also exceed the net all-wave radiation nearly all year round. Modelled building anthropogenic heat fluxes remain similar once the mean daily air temperature exceeds a threshold of about $17.5\text{ }^{\circ}\text{C}$. A monthly time scale analysis of energy balance closure, initially gives a constantly positive residual ($0.7\text{--}8.9\text{ MJ d}^{-1}\text{ m}^{-2}$); whereas accounting for a measurement underestimation of the EC fluxes (20%) and an over-estimation of Q_F (26%) the mean annual residual is effectively zero.

To improve understanding of the role of the storage heat flux in such dense urban settings, more work is needed to better characterise the scale dependence of all fluxes and to quantify the uncertainty of EC observations over complex surfaces. Also, the consideration of various source areas and closer to real-time estimates of the anthropogenic heat flux are required. In a companion paper (Kotthaus and Grimmond, 2013) detailed footprint analysis and the role of surface controls are discussed.

Acknowledgements

This study was funded by EUFP7 Grant agreement no. 211345 (BRIDGE) and NERC ClearLo (NE/H003231/1), supported by NERC ARSF (GB08/19), EPSRC (EP/I00159X/1, EP/I00159X/2) Materials Innovation Hub and KCL. We thank Dr Arnold Moene at Wageningen University for providing the EC-pack software and for all advice regarding its usage; Dr Jiangping He for support of our data archive; Dr Catherine Souch and Dr Helen Ward for their comments; all the many people/students at KCL who contributed to the data collection; KCL Directorate of Estates & Facilities for giving us the opportunity

to operate the various measurement sites. We appreciate the constructive comments and suggestions of both reviewers, which proved very helpful in the development of this work.

References

- Arnfield, A.J., 2003. Two decades of urban climate research: a review of turbulence, exchanges of energy and water, and the urban heat island. *Int. J. Climatol.* 23, 1–26.
- Arnold, S.J., ApSimon, H., Barlow, J., Belcher, S., Bell, M., Boddy, J.W., Britter, R., Cheng, H., Clark, R., Colville, R.N., Dimitroulopoulou, S., Dobre, A., Grealley, B., Kaur, S., Knights, A., Lawton, T., Makepeace, A., Martin, D., Neophytou, M., Neville, S., Nieuwenhuijsen, M., Nickless, G., Price, C., Robins, A., Shallcross, D., Simmonds, P., Smalley, R.J., Tate, J., Tomlin, A.S., Wang, H., Walsh, P., 2004. Introduction to the DAPPLE Air Pollution Project. *Sci. Total Environ.* 332, 139–153.
- Atkinson, B.W., 1969. A further examination of the urban maximum of thunder rainfall in London, 1951–60. *Trans. Inst. Br. Geogr.*, 97–119.
- Bohnstengel, S.I., Evans, S., Clark, P.A., Belcher, S.E., 2011. Simulations of the London urban heat island. *Quart. J. R. Meteorol. Soc.* 137, 1625–1640.
- Chemel, C., Sokhi, R.S., 2012. Response of London's urban heat island to a marine air intrusion in an easterly wind regime. *Boundary Layer Meteorol.* 144, 65–81.
- Christen, A., Vogt, R., 2004. Energy and radiation balance of a Central European City. *Int. J. Climatol.* 24, 1395–1421.
- Coutts, A.M., Beringer, J., Tapper, N.J., 2007. Impact of increasing urban density on local climate: spatial and temporal variations in the surface energy balance in Melbourne. *Aust. J. Appl. Meteorol. Clim.* 46, 477–493.
- Culf, A.D., Foken, T., Gash, J.H.C., 2004. The energy balance closure problem. In: Kabat, P., Claussen, M., Dirmeyer, P.A. (Eds.), *A New Perspective on an Interactive System*. Springer, Berlin, Heidelberg, pp. 159–166.
- Dragonì, D., Schmid, H.P., Grimmond, C.S.B., Loescher, H.W., 2007. Uncertainty of annual net ecosystem productivity estimated using eddy covariance flux measurements. *J. Geophys. Res.* 112, 1–9.
- Flerchinger, G.N., Xie, W., Marks, D., Sauer, T.J., Yu, Q., 2009. Comparison of algorithms for incoming atmospheric long-wave radiation. *Water Resour. Res.* 45, W03423.
- Foken, T., 2008. The energy balance closure problem: an overview. *Ecol. Appl.* 18, 1351–1367.
- Foken, T., Wimmer, F., Mauder, M., Thomas, C., Liebethal, C., 2006. Some aspects of the energy balance closure problem. *Atmos. Chem. Phys.* 6, 4395–4402.
- Fortuniak, K., Pawlak, W., Siedlecki, M., Zieliński, M., 2012. Urban flux measurements in Łódź, central Poland. *FLUXLETTER*, the Newsletter of FLUXNET 5 (1), 14–20.
- Frey, C.M., Parlow, E., Vogt, R., Harhash, M., Abdel Wahab, M.M., 2011. Flux measurements in Cairo. Part 1: in situ measurements and their applicability for comparison with satellite data. *Int. J. Climatol.* 31, 218–231.
- GLA, 2011. *The London Plan*. URL <www.london.gov.uk/publication/londonplan> (accessed 03.05.13).
- GLA, 2012. *Daytime Population, Borough*. URL <<http://data.london.gov.uk/datastore/package/daytime-population-borough>> (accessed 02.11.13).
- Goldbach, A., Kuttler, W., 2012. Quantification of turbulent heat fluxes for adaptation strategies within urban planning. *Int. J. Climatol.* 33, 143–159.
- Grimmond, C.S.B., 1992. The suburban energy balance: methodological considerations and results for a mid-latitude west coast city under winter and spring conditions. *Int. J. Climatol.* 12, 481–497.
- Grimmond, C.S.B., 2006. Progress in measuring and observing the urban atmosphere. *Theor. Appl. Climatol.* 84, 3–22.
- Grimmond, C.S.B., Cleugh, H.A., Oke, T.R., 1991. An objective urban heat storage model and its comparison with other schemes. *Atmos. Environ.* 25B, 311–326.
- Grimmond, C.S.B., Oke, T.R., 1995. Comparison of heat fluxes from summertime observations in the suburbs of four North American cities. *J. Appl. Meteorol.* 34, 873–889.
- Grimmond, C.S.B., Oke, T.R., 1999. Heat storage in urban areas: local-scale observations and evaluation of a simple model. *J. Appl. Meteorol.* 38, 922–940.
- Grimmond, C.S.B., Oke, T.R., 2002. Turbulent heat fluxes in urban areas: observations and a local-scale urban meteorological parameterization scheme (LUMPS). *J. Appl. Meteorol.* 41, 792–810.
- Grimmond, C.S.B., Roth, M., Oke, T.R., Au, Y.C., Best, M., Betts, R., Carmichael, G., Cleugh, H., Dabberdt, W., Emmanuel, R., Freitas, E., Fortuniak, K., Hanna, S., Klein, P., Kalkstein, L.S., Liu, C.H., Nickson, A., Pearlmutter, D., Sailor, D., Voogt, J., 2010. Climate and more sustainable cities: climate information for improved planning and management of cities (producers/capabilities perspective). *Proc. Environ. Sci.* 1, 247–274.
- Grimmond, C.S.B., Salmond, J.A., Oke, T.R., Offerle, B., Lemonsu, A., 2004. Flux and turbulence measurements at a dense urban site in Marseille: heat, mass (water, carbon dioxide) and momentum. *J. Geophys. Res. Atmos.* 109, 19.
- Harrison, R.M., Dal'Osto, M., Beddows, D.C.S., Thorpe, A.J., Bloss, W.J., Allan, J.D., Coe, H., Dorsey, J.R., Gallagher, M., Martin, C., Whitehead, J., Williams, P.L., Jones, R.L., Langridge, J.M., Benton, A.K., Ball, S.M., Langford, B., Hewitt, C.N., Davison, B., Martin, D., Petersson, K.F., Henshaw, S.J., White, I.R., Shallcross, D.E., Barlow, J.F., Dunbar, T., Davies, F., Nemitz, E., Phillips, G.J., Helfter, C., Di Marco, C.F., Smith, S., 2012. Atmospheric chemistry and physics in the atmosphere of a developed megacity (London): an overview of the REPAREE experiment and its conclusions. *Atmos. Chem. Phys.* 12, 3065–3114.
- Helfter, C., Famulari, D., Phillips, G.J., Barlow, J.F., Wood, C.R., Grimmond, C.S.B., Nemitz, E., 2011. Controls of carbon dioxide concentrations and fluxes above central London. *Atmos. Chem. Phys.* 11, 1913–1928.
- Hollinger, D.Y., Richardson, A.D., 2005. Uncertainty in eddy covariance measurements and its application to physiological models. *Tree Physiol.* 25, 873–885.
- Howard, L., 1818. *The Climate of London*, vol. I. W. Phillips, London, p. 346.
- Howard, L., 1833. *The Climate of London*, vols. I–III. Harvey and Darton, London, p. 383.
- Iamarino, M., Beevers, S., Grimmond, C.S.B., 2012. High-resolution (space, time) anthropogenic heat emissions: London 1970–2025. *Int. J. Climatol.* 32, 1754–1767.

- Järvi, J., Hannuniemi, H., Hussein, T., Junninen, H., Aalto, P.P., Hillamo, R., Mäkelä, T., Keronen, P., Siivola, E., Vesala, T., Kulmala, M., 2009. The urban measurement station SMEAR III: continuous monitoring of air pollution and surface–atmosphere interactions in Helsinki, Finland. *Boreal Environ. Res.* 14 (Suppl. i), 86–109.
- Kotthaus, S., Grimmond, C.S.B., 2012. Identification of Micro-scale Anthropogenic CO₂, heat and moisture sources – processing eddy covariance fluxes for a dense urban environment. *Atmos. Environ.* 57, 301–316.
- Kotthaus, S., Grimmond, C.S.B., 2013. Energy exchange in a dense urban environment – Part II: Impact of spatial heterogeneity of the surface. *Urban Climate* 10 (P2) 281–307.
- Langford, B., Nemitz, E., House, E., Phillips, G.J., Famulari, D., Davison, B., Hopkins, J.R., Lewis, A.C., Hewitt, C.N., 2010. Fluxes and concentrations of volatile organic compounds above central London, UK. *Atmos. Chem. Phys.* 10, 627–645.
- Lindberg, F., Grimmond, C., Yogeswaran, N., Kotthaus, S., He, J., Allen, L., Iamarino, M., 2013. Impact of urban changes and weather on anthropogenic heat flux in Europe 1995–2015. *Urban Clim.* 4, 1–15.
- Loridan, T., Grimmond, C.S.B., 2012. Characterization of energy flux partitioning in urban environments: links with surface seasonal properties. *J. Appl. Meteorol. Climatol.* 51, 219–241.
- Loridan, T., Lindberg, F., Jorba, O., Kotthaus, S., Grossman-Clarke, S., Grimmond, C.S.B., 2013. High resolution simulation of the variability of surface energy balance fluxes across central London with urban zones for energy partitioning. *Boundary Layer Meteorol.* 147, 493–523.
- Masson, V., Gomes, L., Pigeon, G., Lioussé, C., Pont, V., Lagouarde, J.-P., Voegt, J., Salmond, J., Oke, T.R., Hidalgo, J., Legain, D., Garrouste, O., Lac, C., Connan, O., Briottet, X., Lachérade, S., Tulet, P., 2008. The canopy and aerosol particles interactions in Toulouse Urban Layer (CAPITTOUL) experiment. *Meteorol. Atmos. Phys.* 102, 135–157.
- Met Office, 2012. Regional Climates: Southern England. URL: <<http://www.metoffice.gov.uk/climate/uk/so/>> (accessed 03.05.13).
- Met Office, 2013. Meeting on UK's run of unusual seasons. met office news. URL: <<http://metofficenews.wordpress.com/2013/06/>> (accessed 07.18.13).
- Michel, D., Philipona, R., Ruckstuhl, C., Vogt, R., Vuilleumier, L., 2008. Performance and uncertainty of CNR1 net radiometers during a one-year field comparison. *J. Atmos. Oceanic Technol.* 25, 442–451.
- Mills, G., 2008. Luke Howard and the climate of London. *Weather* 63, 153–157.
- Moriwaki, R., Kanda, M., 2004. Seasonal and diurnal fluxes of radiation, heat, water vapor, and carbon dioxide over a suburban area. *J. Appl. Meteorol.* 43, 1700–1710.
- Münkel, C., Eresmaa, N., Räsänen, J., Karppinen, A., 2006. Retrieval of mixing height and dust concentration with lidar ceilometer. *Boundary Layer Meteorol.* 124, 117–128.
- Nordbo, A., Järvi, L., Haapanala, S., Moilanen, J., Vesala, T., 2012. Intra-city variation in urban morphology and turbulence structure in Helsinki, Finland. *Boundary Layer Meteorol.* 146, 469–496.
- Offerle, B., Grimmond, C.S.B., Fortuniak, K., 2005. Heat storage and anthropogenic heat flux in relation to the energy balance of a central European city centre. *Int. J. Climatol.* 25 (10), 1405–1419.
- Offerle, B., Grimmond, C.S.B., Fortuniak, K., Klysiak, K., Oke, T.R., 2006a. Temporal variations in heat fluxes over a central European city centre. *Theor. Appl. Climatol.* 84, 103–115.
- Offerle, B., Grimmond, C.S.B., Fortuniak, K., Pawlak, W., 2006b. Intraurban differences of surface energy fluxes in a central European city. *J. Appl. Meteorol.* 45, 125–136.
- Office for National Statistics, 2012. Annual Mid-year Population Estimates for England and Wales, Mid 2011. URL: <<http://www.ons.gov.uk/ons/rel/pop-estimate/population-estimates-for-england-and-wales/mid-2011-2011-census-based/-stb-mid-2011-census-based-population-estimates-for-england-and-wales.html>> (accessed 11.14.12).
- Oke, T.R., 1987. *Boundary Layer Climates*, 2nd ed. London and John Wiley & Sons, New York, Co-published by Routledge, p. 435.
- Pawlak, W., Fortuniak, K., Siedlecki, M., 2011. Carbon dioxide flux in the centre of Lodz, Poland – analysis of a 2-year eddy covariance measurement data set. *Int. J. Climatol.* 31, 232–243.
- Quah, A.K.L., Roth, M., 2011. Diurnal and weekly variation of anthropogenic heat emissions in a tropical city, Singapore. *Atmos. Environ.* 46, 92–103.
- Roberts, S.M., 2010. Three-dimensional radiation flux source areas in urban areas. University of British Columbia, p. 214.
- Robins, A., 2008. DAPPLE (dispersion of air pollution and its penetration into the local environment) experiments and modelling. HPA Chem. Hazards Poisons Rep. 13, 24–28.
- Sailor, D.J., Lu, L., 2004. A top-down methodology for developing diurnal and seasonal anthropogenic heating profiles for urban areas. *Atmos. Environ.* 38, 2737–2748.
- Spronken-Smith, R.A., Kossmann, M., Zawar-Reza, P., 2006. Where does all the energy go? surface energy partitioning in suburban Christchurch under stable wintertime conditions. *Theor. Appl. Climatol.* 84, 137–149.
- Stewart, I.D., Oke, T.R., 2012. “Local Climate Zones” for urban temperature studies. *Bull. Am. Meteorol. Soc.* 93, 1879–1900.
- van Dijk, A., Moene, A.F., de Bruin, H.A.R., 2004. *The Principles of Surface Flux Physics: Theory, Practice and Description of the ECPACK library*. Internal Report, Meteorology and Air Quality Group. Wageningen University, Wageningen, the Netherlands, p. 99.
- Velasco, E., Pressley, S., Allwine, E., Westberg, H., Lamb, B., 2005. Measurements of CO₂ fluxes from the Mexico City urban landscape. *Atmos. Environ.* 39, 7433–7446.
- Vesala, T., Järvi, L., Launiainen, S., Sogachev, A., Rannik, U., Mammarella, I., Siivola, E., Keronen, P., Rinne, J., Riikonen, A., Nikimaa, E., 2008. Surface–atmosphere interactions over complex urban terrain in Helsinki, Finland. *Tellus* 60B, 188–199.
- Ward, H.C., Evans, J.G., Grimmond, C.S.B., 2013. Multi-season eddy covariance observations of energy, water and carbon fluxes over a suburban area in Swindon, UK. *Atmos. Chem. Phys.* 13, 4645–4666.
- Weber, S., Kordowski, K., 2010. Comparison of atmospheric turbulence characteristics and turbulent fluxes from two urban sites in Essen, Germany. *Theor. Appl. Climatol.* 102, 61–74.
- Wood, C.R., Lacser, A., Barlow, J.F., Padhra, A., Belcher, S.E., Nemitz, E., Helfter, C., Famulari, D., Grimmond, C.S.B., 2010. Turbulent flow at 190 m height above London during 2006–2008: a climatology and the applicability of similarity theory. *Boundary Layer Meteorol.* 137, 77–96.